

# Doubly resonant sub-ppt photoacoustic gas detection with eight decades dynamic range

**Zhen Wang**

Changchun Institute of Optics, Fine Mechanics and Physics, Chinese Academy of Sciences

**Hui Zhang**

Changchun Institute of Optics, Fine Mechanics and Physics, Chinese Academy of Sciences

**Qiang Wang**

Changchun Institute of Optics, Fine Mechanics and Physics, Chinese Academy of Sciences

**Simone Borri**

CNR-INO - Istituto Nazionale di Ottica <https://orcid.org/0000-0001-8471-2803>

**Iacopo Galli**

CNR

**Paolo De Natale**

CNR <https://orcid.org/0000-0002-3308-8569>

**Wei Ren** (✉ [renwei@mae.cuhk.edu.hk](mailto:renwei@mae.cuhk.edu.hk))

The Chinese University of Hong Kong <https://orcid.org/0000-0001-6681-593X>

---

## Article

**Keywords:** gas detection, sensors, dynamic range

**Posted Date:** May 18th, 2021

**DOI:** <https://doi.org/10.21203/rs.3.rs-431688/v1>

**License:**   This work is licensed under a Creative Commons Attribution 4.0 International License.

[Read Full License](#)

---

# Abstract

Gas sensors with high sensitivity, wide dynamic range, high selectivity, fast response, and small footprint are desirable across a broad range of applications in energy, environment, safety, and public health. However, designing a compact gas sensor with ultra-high sensitivity and ultra-wide dynamic range remains a challenge. Laser-based photoacoustic spectroscopy (PAS) is a promising candidate to fill this gap. Herein, we report a novel method to simultaneously enhance the acoustic and light waves for PAS using integrated optical and acoustic resonators. This increases sensitivity by more than two orders of magnitude and extends the dynamic range by more than three orders of magnitude, compared with the state-of-the-art photoacoustic gas sensors. We demonstrate the concept by exploiting a near-infrared absorption line of acetylene ( $C_2H_2$ ) at 1531.59 nm, achieving a detection limit of 0.5 parts-per-trillion (ppt), a noise equivalent absorption (NEA) of  $5.7 \times 10^{-13} \text{ cm}^{-1}$  and a linear dynamic range of eight orders of magnitude. This study enables the realization of compact ultra-sensitive and ultra-wide-dynamic-range gas sensors in a number of different fields.

## Introduction

Gas detection plays a significant role in almost all aspects of our modern society such as energy, environment, transportation, agriculture, safety, and security. Among many different types of gas sensors, laser-based ones are best suited to provide several combined key features: accuracy, sensitivity, selectivity, portability, fast response, and safety. By measuring light attenuation through a gas sample, quantitative gas analysis can be performed using the Beer-Lambert law. These optical sensors are increasingly required in a number of fields, including environmental monitoring [1,2], marine science [3,4], biological studies [5,6], and breath analysis [7,8]. State-of-the-art laser absorption sensors using a multipass cell can achieve a noise equivalent absorption (NEA) as low as  $10^{-10} \text{ cm}^{-1}$  with an effective path length of hundred meters [9]. To further enhance sensitivity, the absorption path length can be increased to kilometers by using a high-finesse optical cavity. Among the most sensitive laser-based gas sensing techniques, noise-immune cavity-enhanced optical heterodyne spectroscopy (NICE-OHMS) achieved a NEA of  $10^{-14} \text{ cm}^{-1}$  when operating at an extremely low pressure of 1.8 mTorr [10]; the minimum detectable concentration of a specific molecule has been achieved by saturated-absorption cavity ring-down (SCAR) with a limit of a few parts-per-quadrillion (ppq) [6, 11]. However, the linear dynamic range of this class of optical gas sensors is generally limited to 4-5 orders of magnitude and the overall footprint and weight are still quite large for many applications requiring very compact analyzers. Therefore, numerous applications require versatile gas sensors that can detect sub-part-per-billion (ppb) background concentration in ambient and hundred parts-per-million (ppm) concentration in the target emission, as well.

To get a combined high sensitivity and wide dynamic range, photoacoustic spectroscopy (PAS) is a promising candidate. Indeed, the photoacoustic signal linearly increases with the absorbed laser power, rather than undergoing significant power attenuation after a long absorption path. Instead of directly

measuring light attenuation, PAS relies on the detection of acoustic waves generated in the vibrational relaxation process of molecules excited by photon absorption. Photoacoustic gas sensors also inherit the advantages of high selectivity, high sensitivity, and fast response, like other laser-based spectroscopic methods. In particular, the use of acoustic transducers instead of photodetectors makes PAS sensors more compatible with various laser wavelengths, as sensitive photodetectors are not always available over a wide wavelength range. To date, numerous studies have been focused on advancing PAS by designing new photoacoustic cells, inventing new acoustic transducers, and using different laser sources [12-19]. State-of-the-art PAS-based gas sensors have detection sensitivity between  $10^{-8}$  and  $10^{-11}$  cm<sup>-1</sup> in NEA and a linear dynamic range of five orders of magnitude [20-24].

In this work, we report a PAS sensor with opto-acoustic resonance enhancement for ultra-sensitive and ultra-wide-dynamic-range gas detection. The novel photoacoustic detection module consists of a high-Q-factor acoustic resonator placed inside an optical resonator for the significant amplification of the photoacoustic signal (Fig. 1). A novel photoacoustic design, leveraging on a double standing wave effect, achieves a combined acoustic amplification factor of 175 times and laser power enhancement of almost three orders of magnitude. Using a near-infrared diode laser at 1531.59 nm as a proof-of-principle, we show that our acetylene (C<sub>2</sub>H<sub>2</sub>) sensor reaches a record sensitivity of  $10^{-13}$  cm<sup>-1</sup> (NEA) and an unprecedented linear dynamic range of eight orders of magnitude. Moreover, the C<sub>2</sub>H<sub>2</sub> sensor is validated in a relevant environment to measure ambient background concentration.

## Results

**Theory.** Figure 1 shows the basics of opto-acoustic resonance for PAS. The core gas sensing element consists of an optical resonator, an acoustic resonator, and an acoustic transducer, which are arranged in a coupled configuration. Indeed, when the optical frequency of the incident laser is in resonance with a longitudinal cavity mode of the optical resonator, a standing optical wave is formed between the resonator mirrors. A high-finesse optical resonator can significantly build up the laser power, by several orders of magnitude [25], directly enhancing the photoacoustic signal which scales linearly with the laser power. The laser intensity is modulated at the same resonance frequency as the acoustic resonator. A specifically designed one-dimensional longitudinal tube can be used to amplify the acoustic signal by forming a standing acoustic wave inside it. Any types of acoustic transducers can be used to detect the amplified acoustic wave. In this work, we use both a quartz tuning fork (QTF), resonant at the same frequency as the acoustic resonator, and an electret microphone for demonstration. As shown in Fig. 1, the QTF locates nearby the antinode of the standing acoustic wave, which is generated by the acoustic resonator composed of two stainless-steel tubes placed at the opposite sides of the QTF [26]. The other photoacoustic sensor configuration using an electret microphone is described in the Supplementary Note 3.

The frequency-dependent photoacoustic signal ( $S$ ) at its resonant frequency  $f$  is given by:

$$S = b \times g \times K \times W_{in}(\lambda) \left(1 - e^{-\alpha_{eff}(\lambda)}\right) \varepsilon(f, \tau(P)) \quad (1)$$

where  $b$  is the laser power buildup factor,  $g$  is the acoustic wave enhancement factor,  $K$  is the sensor constant,  $W_{in}$  is the incident laser power,  $\lambda$  is the laser wavelength,  $\alpha_{eff}(\lambda)$  is the effective absorbance by the analyte,  $\tau(P)$  is the relaxation time at the gas pressure  $P$ , and  $\varepsilon$  is the radiation-to-sound conversion efficiency [27], which depends on  $f$  and  $\tau$ . Note that the factor  $g$  is independent of laser power but is related to the geometry, to the material, and to the Q-factor of the acoustic resonator, as well as to the frequency of sound waves [28]. The power buildup factor  $b$  is determined by the finesse of the optical resonator, which needs to be properly selected so that a wide linear dynamic range and a high sensitivity can be simultaneously obtained (see Methods).

**Experimental setup.** The schematic of the PAS sensor is shown in Fig. 2. An external cavity diode laser (ECDL) is used to detect the P(11) line of  $C_2H_2$  at 1531.59 nm. The ECDL is phase modulated by an electro-optic modulator (EOM) at 20 MHz and locked to the optical resonator using the Pound-Drever-Hall (PDH) method [29]. Details of the application of the PDH method to PAS can be found in [24]. In this work, the current and piezo transducer (PZT) feedback loops are both used for a more robust locking performance. Each mirror of the optical resonator has a radius of curvature of 150 mm and reflectivity of 99.923% (finesse 4078) at the laser wavelength, as measured by cavity ring-down (see Supplementary Note 1). Compared with other cavity-enhanced absorption spectroscopic methods [6,10], the optical resonator used here for the opto-acoustic resonance features a much shorter length (60 mm in this work). Two mode matching lenses ( $f_1$  and  $f_2$ ) are used to maximize the coupling efficiency (84%) between the laser and the optical resonator (see Supplementary Note 2). With a maximum incident laser power of 300 mW, the intracavity optical power is boosted to 264 W in this work (see Methods).

The intracavity laser beam passes through the acoustic resonator, consisting of two stainless-steel tubes (inner diameter 1.3 mm, length 23 mm), and does not touch any surface. The central axis of the acoustic resonator is about 1.2 mm below the top of the QTF prongs, thus optimizing the piezoelectrical conversion efficiency [15]. The two tubes are placed at a distance of  $\sim 60 \mu\text{m}$  from the QTF, so that it lies near the antinode of the acoustic wave and leaves its Q-factor unaffected. The beam waist ( $340 \mu\text{m}$  in diameter) is located between the two prongs of the QTF, which has a resonant frequency of 7.2 kHz and a Q-factor  $\sim 8000$  (gas pressure 760 Torr) [15]. Photoacoustic gas sensors using QTF as an acoustic transducer have been previously developed for detecting many different gas species [15-17]. The optical resonator, the acoustic resonator and the QTF are all enclosed inside a chamber. A high-speed lithium niobate optical switch is used to chop the laser beam at the same frequency as the resonant frequency of the QTF. The piezoelectric current from the QTF is collected by a trans-impedance amplifier and then amplified by a low-noise voltage preamplifier. Finally, a lock-in amplifier with a detection bandwidth of 1 Hz is used to demodulate the first harmonic signal (1f) at the sensor output.

**Double standing wave enhancement.** To evaluate the enhancement effects due to the integrated acoustic and optical resonators, the PAS-1f signal of the  $C_2H_2$  line at 1531.59 nm is measured under three

different configurations. Figure 3 compares the typical PAS-1f signal measured using a bare QTF (2% C<sub>2</sub>H<sub>2</sub>), a QTF with the mere acoustic resonator (0.1% C<sub>2</sub>H<sub>2</sub>), and a QTF with the complete opto-acoustic resonator (1 ppm C<sub>2</sub>H<sub>2</sub>). Note that different C<sub>2</sub>H<sub>2</sub> concentrations are used for these three configurations because of their quite different sensitivity. All the experiments are performed at the same incident laser power of 12 mW, lock-in detection bandwidth of 1 Hz, and gas pressure of 760 Torr. After normalization by the gas concentration, a comparison of Fig. 3(a) and Fig. 3(b) shows that the acoustic resonator enhances the PAS-1f signal by 175 times. Besides, the optical resonator provides another enhancement factor of 980, as emerging from a comparison of Fig. 3(b) and Fig. 3(c). Hence, the combined opto-acoustic amplification provides an overall enhancement of the PAS signal by a factor of 10<sup>5</sup> via the double standing wave effect.

**Ultra-sensitive gas detection.** Figure 4 shows the PAS-1f signal measured by the photoacoustic sensor for an incident optical power of 12 mW. The measurement is performed at 760 Torr for different C<sub>2</sub>H<sub>2</sub> concentrations (100 ppb and 10 ppb in nitrogen balance) and high-purity nitrogen (99.999% purity) when the laser wavelength is tuned from 1531.32 nm to 1531.75 nm. The peak values at 1531.59 nm are 4.05 mV (100 ppb C<sub>2</sub>H<sub>2</sub>) and 0.68 mV (10 ppb C<sub>2</sub>H<sub>2</sub>), respectively. Note that the background signal is contributed by the thermoelastic effect due to unwanted absorption at the optical window and resonator mirror [30]. This background signal has not been subtracted from the PAS-1f signal shown in Fig. 4. Interestingly, due to the excellent signal-to-noise ratio, a neighboring water line near 1531.37 nm emerges, as shown in Fig. 4(b). This is probably due to residual water in the gas chamber after the desiccation process (see Methods). Our hypothesis is confirmed by repeating the measurement with pure nitrogen (water vapor < 0.3 ppm) shown in Fig. 4(c). To reduce the measurement uncertainty, a multi-spectral fitting method, with prior knowledge of infrared spectra from the HITRAN database [31], is implemented. Hence, the background signal is automatically eliminated during the fitting procedure.

The relationship between the PAS-1f signal and incident laser power is also investigated. Figure 5(a) compares the PAS-1f signal at 1 ppb C<sub>2</sub>H<sub>2</sub> under two different incident power levels (12 mW and 300 mW). The peak value of the PAS-1f signal is increased by a factor of about 22.5 when the incident laser power is increased from 12 mW to 300 mW (a factor of 25). The slight deviation of the enhancement factor between laser power and PAS signal is due to the variation of the optical coupling efficiency. By repeating the measurement at 100 ppb C<sub>2</sub>H<sub>2</sub>, Fig. 5(b) shows the variation of the PAS-1f amplitude with the incident optical power. The sensor signal increases almost linearly (0.25 mV/mW) with the incident power. In contrast, the noise level remains almost unchanged over the entire power range, as shown in Fig. 5(b) (1-σ standard deviation of N<sub>2</sub> over 120 s). This makes this set-up very promising to further increase detection sensitivity by simply increasing the incident laser power.

**Test of dynamic range and detection limit.** The linear response of the sensor is tested at the pressure of 760 Torr by filling the gas chamber with different C<sub>2</sub>H<sub>2</sub>/N<sub>2</sub> mixtures. Fig. 6 shows the background-subtracted PAS-1f amplitude as a function of C<sub>2</sub>H<sub>2</sub> concentration, varying in a 1 ppb-500 ppm interval. The sensor shows a very good linear response with a slope of 36.4 μV/ppb and an R-square value of 0.99

from 1 ppb to 50 ppm. However, the sensor deviates from the linear response at higher  $C_2H_2$  concentrations due to the apparent degradation of optical finesse of the optical resonator.

To evaluate the long-term stability and the minimum detection limit, the Allan–Werle deviation analysis is conducted by measuring nitrogen with the results shown in Fig. 7. The noise equivalent concentration (NEC) is determined to be 5.1 ppt (unity for signal-to-noise ratio) at an integration time of 1 s. At an incident optical power of 300 mW and a detection bandwidth of 1 Hz, we obtain a normalized noise equivalent absorption coefficient (NNEA) of  $1.7 \times 10^{-12} \text{ Wcm}^{-1}\text{Hz}^{-1/2}$  (see Methods). The NEC can be improved to 0.5 ppt at a longer integration time of 300 s, leading to a noise equivalent absorption (NEA) of  $5.7 \times 10^{-13} \text{ cm}^{-1}$ . As a result, the proposed photoacoustic gas sensor achieves a linear dynamic range of  $1.0 \times 10^8$ .

To verify the versatility of this technique, we also develop another photoacoustic sensor by using a conventional longitudinal acoustic resonator with buffering volumes (Q-factor 25), an electret microphone, and a longer optical resonator (80 mm) with the same finesse (see Supplementary Note 3). The microphone-based sensor can be easily aligned along the optical path and a similar performance in terms of sensitivity and dynamic range is demonstrated, as compared to the previous configuration.

The dynamic stability of the sensor is also important for applications requiring continuous gas sampling. This is evaluated by operating the gas sensor when continuously filling  $C_2H_2$  gas samples into the gas chamber. Our sensor behaves well, without any interruption, during the gas filling and flow rate changing processes (see Supplementary Note 4).

## Discussion

The key performance parameters (e.g., linear dynamic range, NEC, and NEA) of some state-of-the-art photoacoustic gas sensors are summarized in Table 1. The photoacoustic gas sensor developed in this work shows an unprecedented linear dynamic range and NEA, superior to the state-of-the-art photoacoustic sensors using different types of laser sources and acoustic transducers. Most remarkably, the current linear dynamic range is three orders of magnitude larger than the state-of-the-art ( $10^5$ ) [20], and the current NEA is two orders of magnitude better than the state-of-the-art ( $10^{-11} \text{ cm}^{-1}$ ) [23]. Besides, our sensor operates at atmospheric pressure, which is more suitable for field applications.

Gas	Method	$\lambda$ ( $\mu\text{m}$ )	Linear dynamic range	NEC (ppt)	NEA ( $\text{cm}^{-1}$ )	Integration time	Pressure (Torr)
$\text{NO}_2$	PAS <sup>[20]</sup>	0.447	$1 \times 10^5$	54	$2.3 \times 10^{-10}$	1 s	640
$\text{SF}_6$	QEPAS <sup>[21]</sup>	10.54	$3.2 \times 10^3$	50	$6.1 \times 10^{-9}$	1 s	75
$\text{CO}_2$	I-QEPAS <sup>[22]</sup>	4.33	$2.8 \times 10^3$	300	$1.4 \times 10^{-8}$	20 s	38
$\text{C}_2\text{H}_2$	CECEPAS <sup>[23]</sup>	1.531	$6.7 \times 10^3$	24	$2.4 \times 10^{-11}$	100 s	150
$\text{C}_2\text{H}_2$	CE-PAS <sup>[24]</sup>	1.531	$1 \times 10^4$	300	$1.9 \times 10^{-10}$	300 s	50
$\text{C}_2\text{H}_2$	This work	1.531	$1 \times 10^8$	0.5	$5.7 \times 10^{-13}$	300 s	760

Note: The linear dynamic range, NEC, and NEA are all the best parameters reported in the relevant studies.

The field performance of this sensor is evaluated by measuring atmospheric  $\text{C}_2\text{H}_2$  concentration in Changchun, Jilin, China. The outdoor air samples are collected in aluminum foil bags and then dehumidified before each measurement inside the gas chamber. By comparing the measured spectra with the HITRAN database, we are able to identify the  $\text{C}_2\text{H}_2$  line at 1531.59 nm and the neighboring spectra of  $\text{CO}_2$  and  $\text{H}_2\text{O}$  centered at 1531.65 nm and 1531.37 nm, respectively, shown in Fig. 8(a). The  $\text{C}_2\text{H}_2$  gas concentration is determined from the calibration curve based on the measured PAS-1f signal shown in Fig. 6. The measured  $\text{C}_2\text{H}_2$  concentration at the same location from 7:00 am to 4:00 am - next day is plotted in Fig. 8(b), showing a variation between 1 ppb and 2 ppb at 23°C and 760 Torr. The shaded area denotes the relative systematic uncertainty, which is evaluated to be 31% by comparing the gas concentration values extracted from the fitting equation with the calibrated gas samples using the gas mixer. Our measurement result is in very good agreement with the previous ambient  $\text{C}_2\text{H}_2$  studies using cavity ring-down spectroscopy, gas chromatographic separation and flame ionization detection (GC-FID) [32,33], but with a better (70-240 times) signal-to-noise ratio.

In summary, we have developed a novel photoacoustic gas sensor using an integrated optical-acoustic resonator. Taking advantage of a double standing wave enhancement, the photoacoustic signal can be improved by five orders of magnitude, thus providing ultra-sensitive gas detection with low-power semiconductor lasers. The moderate cavity finesse maintains the high coupling efficiency of the incident laser and enables a wide linear dynamic range by using a short optical resonator. As a result, we have demonstrated a photoacoustic sensor with a NEC of 0.5 ppt, a NEA of  $5.7 \times 10^{-13} \text{ cm}^{-1}$ , and a linear dynamic range of eight orders of magnitude. Furthermore, we have demonstrated it can work, for atmospheric  $\text{C}_2\text{H}_2$  measurement, in a field application. Although the demonstration is performed in the near-infrared region, the concept can be extended to the mid-infrared range, where many molecules have much stronger absorption bands. Importantly, combined with other light sources such as frequency combs, the new photoacoustic gas sensing technique developed in this work would lead to a powerful analytical tool for rapid and ultra-sensitive detection of multi-species [18].

## Methods

**Selection of finesse for the optical resonator.** The finesse of the optical resonator needs to be properly selected in this work. First, the selection of a higher finesse theoretically provides a larger power enhancement factor. However, the linewidth of the cavity mode decreases with the increased finesse, making it more challenging to achieve a high coupling efficiency of the laser into the optical resonator. Second, the linear dynamic range of the sensor is affected by the finesse. The finesse is determined by the round-trip loss inside the optical resonator which includes the mirror transmission and absorption, gas absorption, and loss induced by the acoustic module. The finesse increases with the larger reflectivity of cavity mirrors, but it decreases apparently when the loss induced by gas absorption becomes comparable. Hence, the physical length of the optical resonator should be selected as short as possible to minimize the gas-absorption loss inside the cavity. In this work, a moderate finesse of about 4000 (mirror reflectivity, 99.923%) and a physical length of 60 mm is used.

**Calibration of intracavity laser power.** According to the main text, the optical resonator enhances the photoacoustic signal by a factor of 980. Considering the 84% coupling efficiency, the intracavity power enhancement factor is 1166, which is slightly lower than the theoretical buildup factor of 1300. This is probably due to the extra cavity loss caused by the QTF. As the empty cavity has a finesse of 4078, an additional loss of 0.017% can deteriorate the buildup factor from 1300 to 1166. When the incident power is adjusted from 12 mW to 300 mW, there is an extra 10% degradation of coupling efficiency. Hence, the maximum of the intracavity power is determined to be 264 W.

**Gas chamber dehumidification.** To mitigate the interference of the residual water molecules inside the vacuum cavity, the gas chamber is heated to 60°C and purged continuously by dry nitrogen for several hours. To protect the QTF which is quite close to the acoustic resonator, the heating temperature is controlled not quite high. It is possible to have some residual water inside the chamber.

**NNEA calculation.** The NNEA coefficient can be calculated by the following equation:

$$NNEA = \frac{\alpha_{min} \times W_{in}}{\sqrt{BW}}$$

where  $\alpha_{min}$  is the noise equivalent absorption (NEA) coefficient,  $W_{in}$  is the incident power and  $BW$  is the detection bandwidth. With the NEC of 5.1 ppt in Fig. 7, NEA can be easily obtained by referencing to the HITRAN database [31]. The incident power is 300 mW. Together with the detection bandwidth of 1 Hz, the NNEA of  $1.7 \times 10^{-12} \text{ Wcm}^{-1} \text{ Hz}^{-1/2}$  can be calculated.

## Declarations

### Data availability

The data that support the findings within this paper are available from the corresponding authors upon reasonable request.

## Acknowledgements

This research was supported by the Strategic Priority Research Program of Chinese Academy of Sciences (XDA17040513, XDA22020502), National Natural Science Foundation of China (NSFC) (51776179, 62005267), General Research Fund (14209220) from the University Grants Committee, Seed Project (ITS/242/19) from the Innovation and Technology Commission. We thank Professor Vincenzo Spagnolo from the Technical University of Bari for providing us the custom QTF.

## Author contributions

Z.W., Q.W. and W.R. conceived the idea, designed the experiments, discussed the results and prepared the manuscript. Z.W. built the systems and conducted the experiments. H.Z. and Q.W. assisted in building the systems and conducting the experiments. S.B., I.G. and P.D.N. assisted in the PDH locking and optical coupling. W.R. and Q.W. supervised and coordinated the project.

## Competing interests

The authors declare no competing interests.

## Additional information

Supplementary information is available for this paper.

Correspondence and requests for materials should be addressed to Q.W. or W.R.

## References

1. Kreuzer, L. B. & Patel, C. K. N. Nitric oxide air pollution: detection by optoacoustic spectroscopy. *Science* **173**, 45-47 (1971).
2. Rieker, G. B. et al. Frequency-comb-based remote sensing of greenhouse gases over kilometer air paths. *Optica* **1**, 290-298 (2014).
3. Kort, E. A. et al. Atmospheric observations of Arctic Ocean methane emissions up to 82 north. *Geosci.* **5**, 318-321 (2012).
4. Thornton, B. F., Prytherch, J., Andersson, K., Brooks, I. M., Salisbury, D., Tjernström, M. & Crill, P. M. Shipborne eddy covariance observations of methane fluxes constrain Arctic sea emissions. *Adv.* **6**, eaay7934 (2020).
5. Adato, R. & Altug, H. In-situ ultra-sensitive infrared absorption spectroscopy of biomolecule interactions in real time with plasmonic nanoantennas. *Commun.* **4**, 1-10 (2013).
6. Galli, I. et al. Spectroscopic detection of radiocarbon dioxide at parts-per-quadrillion sensitivity. *Optica* **3**, 385-388 (2016).
7. Wang, C. & Sahay, P. Breath analysis using laser spectroscopic techniques: breath biomarkers, spectral fingerprints, and detection limits. *Sensors* **9**, 8230-8262 (2009).

8. Thorpe, M. J. et al. Cavity-enhanced optical frequency comb spectroscopy: application to human breath analysis. *Express* **16**, 2387-2397 (2008).
9. Nelson, D. D. et al. Characterization of a near-room-temperature, continuous-wave quantum cascade laser for long-term, unattended monitoring of nitric oxide in the atmosphere. *Lett.* **31**, 2012-2014 (2006).
10. Ye, J., Ma, L. S. & Hall, J. L. Ultrasensitive detections in atomic and molecular physics: demonstration in molecular overtone spectroscopy. *Opt. Soc. Am. B* **15**, 6-15 (1998).
11. Delli Santi, M.G., Bartalini, S., Cancio, P., Galli, I., Giusfredi, G., Haraldsson, C., Mazzotti, D., Pesonen, A. & De Natale, P. Biogenic Fraction Determination in Fuel Blends by Laser-Based  $^{14}\text{CO}_2$  *Adv. Photonics Res.* **2**, 2000069 (2021).
12. Liu, K., Mei, J., Zhang, W., Chen, W. & Gao, X. Multi-resonator photoacoustic spectroscopy. *Actuat. B Chem.* **251**, 632-636 (2017).
13. Wu, H. et al. Beat frequency quartz-enhanced photoacoustic spectroscopy for fast and calibration-free continuous trace-gas monitoring. *Commun.* **8**, 1-8 (2017).
14. Tomberg, T., Vainio, M., Hieta, T. & Halonen, L. Sub-parts-per-trillion level sensitivity in trace gas detection by cantilever-enhanced photo-acoustic spectroscopy. *Rep.* **8**, 1-7 (2018).
15. Wu, H. et al. Quartz enhanced photoacoustic  $\text{H}_2\text{S}$  gas sensor based on a fiber-amplifier source and a custom tuning fork with large prong spacing. *Phys. Lett.* **107**, 111104 (2015).
16. Zheng, H. et al. Single-tube on-beam quartz-enhanced photoacoustic spectroscopy. *Lett.* **41**, 978-981 (2016).
17. Wang, Q., Wang, Z., Ren, W., Patimisco, P., Sampaolo, A. & Spagnolo, V. Fiber-ring laser intracavity QEPAS gas sensor using a 7.2 kHz quartz tuning fork. *Actuat. B Chem.* **268**, 512-518 (2018).
18. Wildi, T., Voumard, T., Brasch, V., Yilmaz, G. & Herr, T. Photo-acoustic dual-frequency comb spectroscopy. *Commun.* **11**, 1-6 (2020).
19. Xiong, L., Bai, W., Chen, F., Zhao, X., Yu, F. & Diebold, G. J. Photoacoustic trace detection of gases at the parts-per-quadrillion level with a moving optical grating. *Natl Acad. Sci.* **114**, 7246-7249 (2017).
20. Yin, X. et al. Sub-ppb nitrogen dioxide detection with a large linear dynamic range by use of a differential photoacoustic cell and a 3.5 W blue multimode diode laser. *Actuat. B Chem.* **247**, 329-335 (2017).
21. Spagnolo, V. et al. Part-per-trillion level  $\text{SF}_6$  detection using a quartz enhanced photoacoustic spectroscopy-based sensor with single-mode fiber-coupled quantum cascade laser excitation. *Lett.* **37**, 4461-4463 (2012).
22. Borri, S. et al. Intracavity quartz-enhanced photoacoustic sensor. *Phys. Lett.* **104**, 091114 (2014).
23. Tomberg, T., Hieta, T., Vainio, M. & Halonen, L. Cavity-enhanced cantileverenhanced photo-acoustic spectroscopy. *Analyst* **144**, 2291–2296 (2019)
24. Wang, Z., Wang, Q., Zhang, W., Wei, H., Li, Y. & Ren, W. Ultrasensitive photoacoustic detection in a high-finesse cavity with Pound–Drever–Hall locking. *Lett.* **44**, 1924-1927 (2019).

25. Friss, A. J., Limbach, C. M. & Yalin, A. P. Cavity-enhanced rotational Raman scattering in gases using a 20 mW near-infrared fiber laser. *Lett.* **41**, 3193-3196 (2016).
26. Dong, L., Kosterev, A. A., Thomazy, D., & Tittel, F. K. QEPAS spectrophones: design, optimization, and performance. *Phys. B* **100**, 627-635 (2010).
27. Russo, S. D. et al. Quartz-enhanced photoacoustic spectroscopy exploiting low-frequency tuning forks as a tool to measure the vibrational relaxation rate in gas species. *Photoacoustics* **21**, 100227 (2021).
28. Miklós, A., Hess, P. & Bozóki, Z. Application of acoustic resonators in photoacoustic trace gas analysis and metrology. *Sci. Instrum.* **72**, 1937-1955 (2001).
29. Drever, R. W. P., Hall, J. L., Kowalski, F. V., Hough, J., Ford, G. M., Munley, A. J., & Ward, H. Laser phase and frequency stabilization using an optical resonator. *Phys. B* **31**, 97-105 (1983).
30. Liu, L., Huan, H., Zhang, X., Zhang, L., Shao, X. & Mandelis, A. Laser Induced Thermoelastic Contributions from Windows to Signal Background in a Photoacoustic Cell. *Photoacoustics* **22**, 100257 (2021).
31. Gordon, I. et al. The HITRAN2016 molecular spectroscopic database. *Quant. Spectrosc. Radiat. Transfer* **203**, 3–69 (2017).
32. Pradhan, M., Lindley, R. E., Grilli, R., White, I. R., Martin, D. & Orr-Ewing, A. J. Trace detection of C<sub>2</sub>H<sub>2</sub> in ambient air using continuous wave cavity ring-down spectroscopy combined with sample pre-concentration. *Phys. B* **90**, 1-9 (2008).
33. Schmidt, F. M., Vaittinen, O., Metsälä, M., Kraus, P. & Halonen, L. Direct detection of acetylene in air by continuous wave cavity ring-down spectroscopy. *Phys. B* **101**, 671-682 (2010).

## Figures

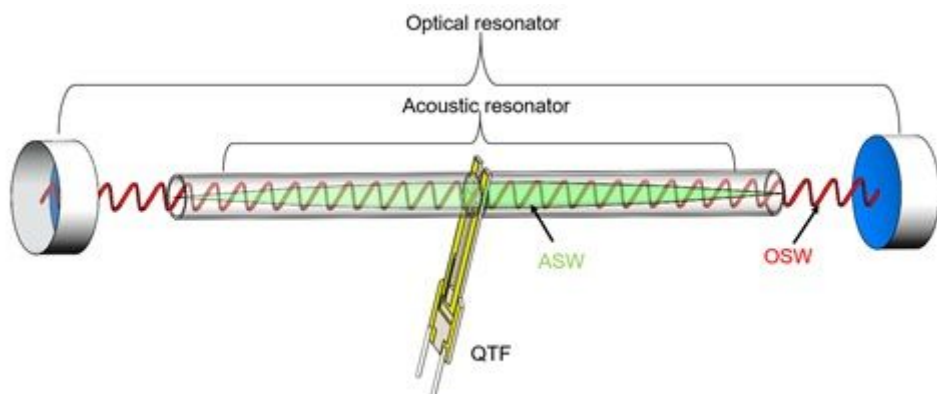


**Figure 1**

Principle of the opto-acoustic resonance for PAS. ASW: acoustic standing wave; OSW: optical standing wave; QTF: quartz tuning fork. The amplitude of the OSW is modulated at the resonant frequency of the QTF. The geometry of the acoustic resonator is designed according to the acoustic frequency.

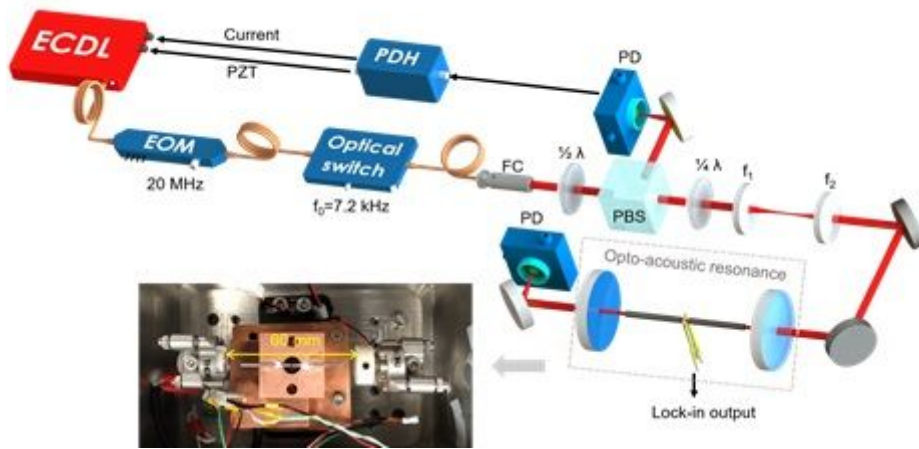


**Figure 2**

Schematic of the photoacoustic sensor with opto-acoustic resonance. ECDL, external cavity diode laser; EOM, electro-optic modulator; FC, fiber collimator;  $1/4 \lambda$ , quarter-wave plate;  $1/2 \lambda$ , half-wave plate; PBS, polarization beam splitter; PD, photodetector; PZT, piezo transducer. The opto-acoustic resonance element has the same configuration as that shown in Fig. 1, which is enclosed in a gas chamber. Inset: photo of the opto-acoustic resonance setup inside the gas chamber.

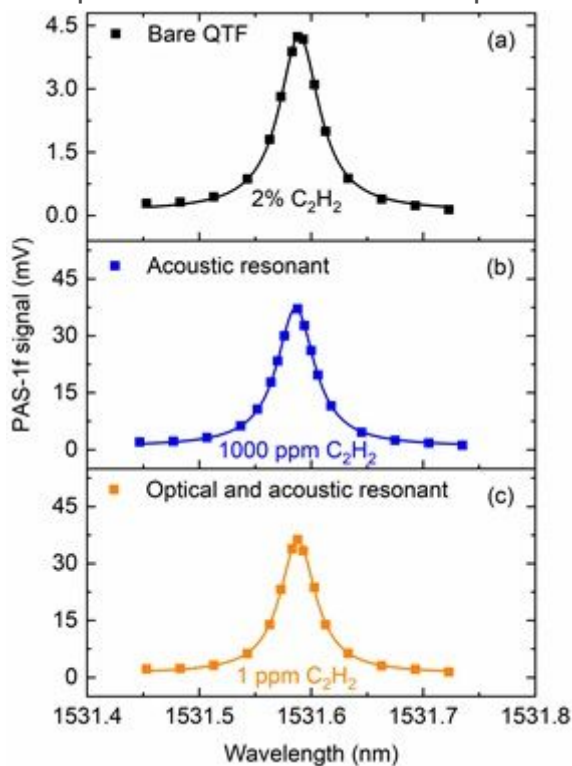


**Figure 3**

PAS-1f signal measured by three different configurations: (a) bare QTF, (b) QTF with acoustic resonator, and (c) QTF with acoustic and optical resonators. The amplitude of the single-pass PAS signal at 2% C<sub>2</sub>H<sub>2</sub> using the bare QTF is about 4.24 mV. Benefitting from the double standing wave enhancement, the

sensor has a response of 36 mV to 1 ppm C<sub>2</sub>H<sub>2</sub>. An enhancement factor up to five orders of magnitude for the PAS signal is achieved.

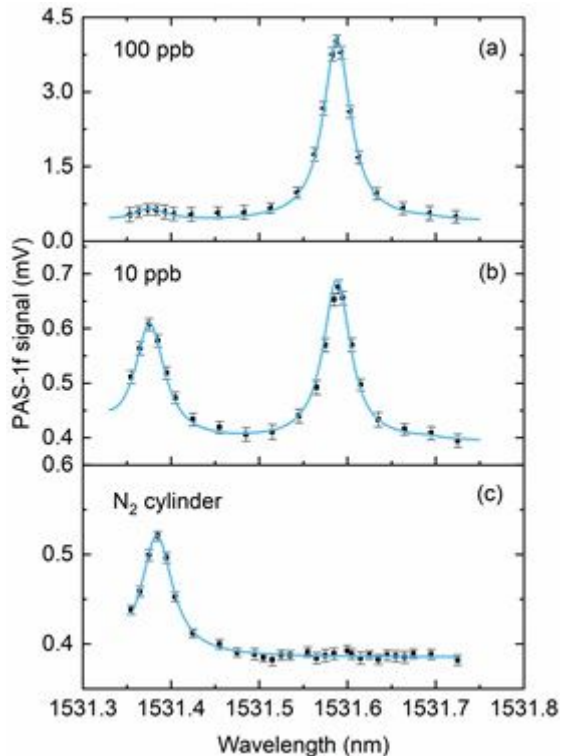


**Figure 4**

Representative PAS-1f signal of C<sub>2</sub>H<sub>2</sub>/N<sub>2</sub> mixtures and N<sub>2</sub> bath gas measured at the pressure of 760 Torr. The target C<sub>2</sub>H<sub>2</sub> peak is observed at 1531.59 nm, whereas another H<sub>2</sub>O line is also evident at 1531.37 nm. The error bars (1- $\sigma$  standard deviation) are calculated from the raw data, taken in a time interval of 120 s; error bars in (a) and (b) are magnified by 20 and 2 times, respectively, for the sake of clarity. The background of the PAS signal (0.4 mV for an incident optical power of 12 mW) is caused by the thermoelastic effect of unwanted light absorption at the optical window and resonator mirrors.

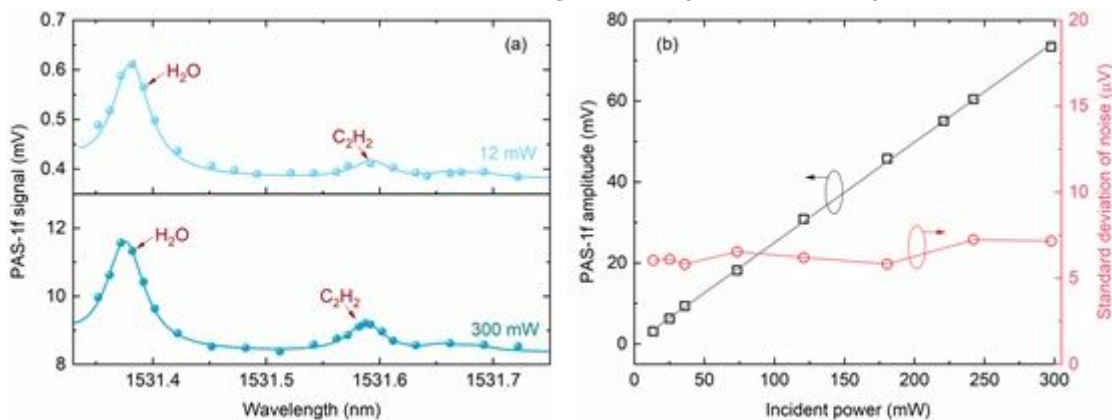


**Figure 5**

(a) Representative PAS-1f signal of 1 ppb C<sub>2</sub>H<sub>2</sub> measured at two different incident optical power levels (12 mW and 300 mW). The background of the PAS signal increases apparently with the incident power.

The PAS-1f amplitudes of 1 ppb C<sub>2</sub>H<sub>2</sub> at different incident power levels need to be inferred from the fitting results. (b) PAS-1f amplitude for 100 ppb C<sub>2</sub>H<sub>2</sub> and 1- $\sigma$  standard deviation of the noise (a measurement of nitrogen over 120 s) versus incident power when the laser is tuned at the absorption line center of C<sub>2</sub>H<sub>2</sub>, at 1531.59 nm. The gas pressure is 760 Torr and the detection bandwidth of the lock-in amplifier is 1 Hz. The linear increase of the PAS-1f amplitude and the almost unchanged noise demonstrate a linear sensitivity enhancement.

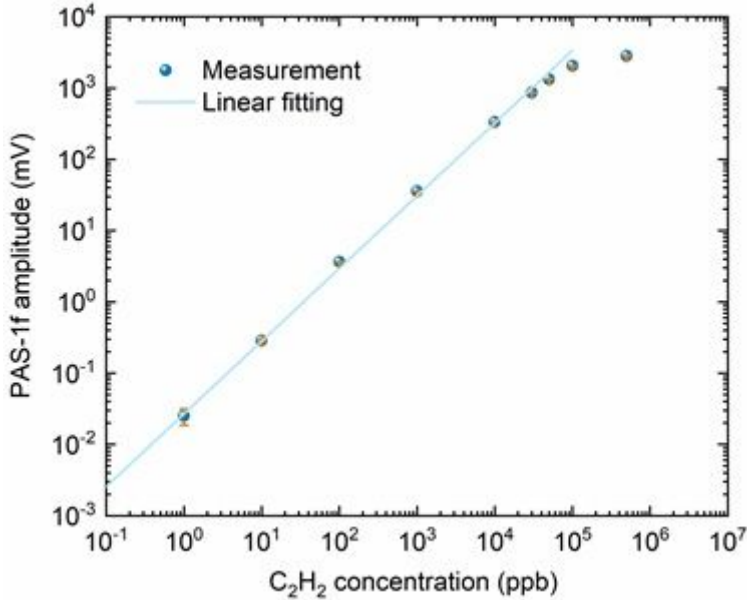


Figure 6

Background-subtracted PAS-1f amplitude as a function of gas concentration for an incident power of 12 mW. The linear fitting yields an R-square value of 0.99 from 1 ppb to 50 ppm. Error bars on the vertical axis show the 1- $\sigma$  standard deviation from over 120 s measurements.

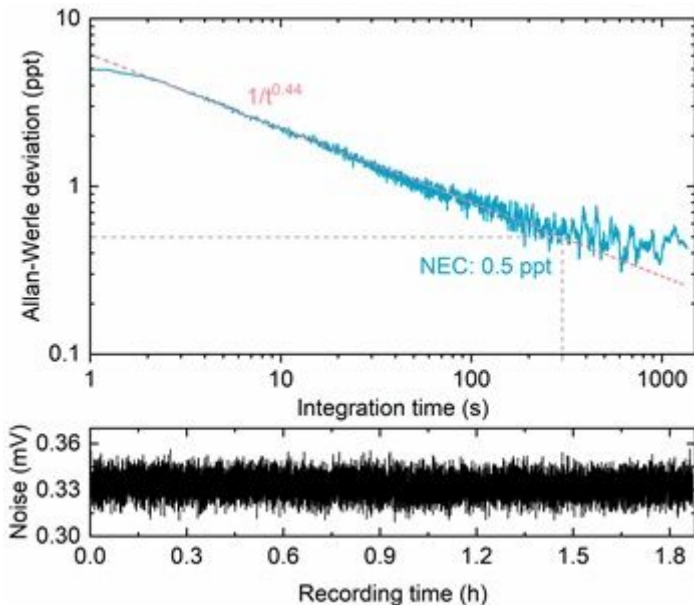
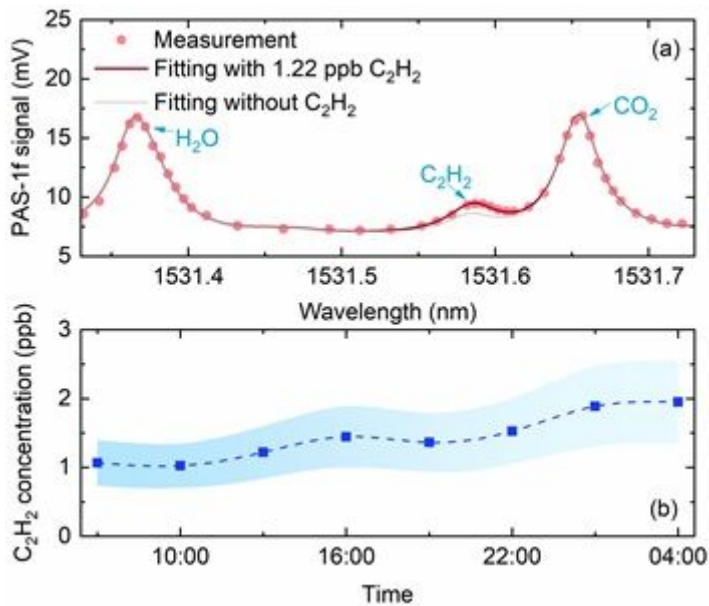


Figure 7

Allan–Werle deviation analysis for the sensor when the laser wavelength is tuned to the peak of the C<sub>2</sub>H<sub>2</sub> absorption line, with the chamber filled with nitrogen. As a function of integration time, the analysis shows the achieved NEC of 0.5 ppt at 300 s. The dashed line in the top panel represents the 1/t<sup>0.44</sup> slope. The bottom panel depicts the raw data of noise measured for nearly 2 hours. The detection bandwidth is the same as the signal measurement.



**Figure 8**

(a) Representative PAS-1f signal of outdoor air in Changchun Institute of Optics, Fine Mechanics and Physics (CIOMP) at 1:00 pm, 16 December, 2020. The residual signal simulated without C<sub>2</sub>H<sub>2</sub> (grey line) at 1531.59 nm is contributed by the ambient CO<sub>2</sub> absorption. (b) Time variation of ambient C<sub>2</sub>H<sub>2</sub> concentration measured in 24 hours. The shaded region represents 31% relative systematic uncertainty in the range of 1-2 ppb, which is evaluated by comparing the calibrated gas samples with our sensor results.

## Supplementary Files

This is a list of supplementary files associated with this preprint. Click to download.

- [Supplementary0416.docx](#)